Geomorphology 500 (2026) 110228

Contents lists available at ScienceDirect

Geomorphology

journal homepage: www.journals.elsevier.com/geomorphology

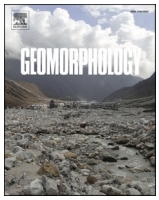

Erosion rates in rock salt exposures with diverse karren monitored by erosion pins, close-range photogrammetry and terrestrial laser scanner

Guillermo Pérez-Villar [a,*], Francisco Gutiérrez [a], Alfonso Benito-Calvo [b], Carles Roqué [c]

[a] Departamento de Ciencias de la Tierra, Universidad de Zaragoza, C/ Pedro Cerbuna 12, 50009, Zaragoza, Spain
[b] CENIEH, Paseo Sierra de Atapuerca 3, Burgos, 09002, Spain
[c] Departamento de Ciencias Ambientales, Facultad de Ciencias, Universitat de Girona, E-17003, Girona, Spain

ARTICLE INFO

Keywords:
Salt karst
Solutional erosion
Karren
Salt diapir

ABSTRACT

Published data on solutional erosion in rock salt exposures are scarce, hindering our ability to understand the evolution of emergent salt diapirs with a number of practical implications (e.g. long-term geostorage). The Bofia Gran karst depression at the actively rising Cardona salt diapir (NE Spain) has been used as a test site to assess chemical erosion on a salt outcrop with a wide diversity of karren. Denudation measurements obtained by using erosion pins, terrestrial laser scanner (TLS) and ground-based photogrammetry consistently indicate a robust relationship between rainfall and slope-normal erosion, with an average value of around 10 mm per 100 mm rainfall. The significant variability observed in the surface-normal erosion is mainly controlled by slope gradient and karren micro-topography. Surface-normal erosion increases linearly as the slope declines and the surface area that interacts with rainfall decreases. The comparison of high-resolution point clouds shows that the range of erosion values across specific karren increases with their complexity, with extreme situations found in planar solution bevels and rugged solution flutes. The empirical relationships between slope-normal erosion and both rainfall and slope can be used to model geomorphic evolution in rock salt exposures, as illustrated with the case of the Bofia Gran, where diapiric uplift overwhelms chemical erosion. The experience gained in this investigation suggests that photogrammetry using a conventional camera can be more effective than TLS for assessing erosion in areas on the order of square meters. It also illustrates the benefits of using erosion values normalized to precipitation to enable worldwide comparisons.

1. Introduction

Erosion or denudation refers to the removal of mass as solid particles and dissolved material by a suite of physical, chemical, and biotic processes (Gaillardet, 2004; Lupia-Palmieri, 2004). In karst terrains, underlain by soluble rocks and often dominated by subsurface drainage, chemical erosion prevails and a significant part of the mass removal may occur in the subsurface (Gunn, 2013). Attempts have been made in a significant number of studies to assess erosion by direct methods (e.g., surface lowering, weight loss of standard tablets) on carbonate rocks and gypsum, typically facing problems associated with the slowness of the process at a human time-scale (see review in De Waele and Gutiérrez, 2022). Nonetheless, solutional erosion on rock salt exposures, given the high solubility of halite (356 g/L; mass of solute in 1 L of solvent), is a very rapid process that can be satisfactorily measured over short periods of time. Despite the suitability of rock salt exposures for erosion assessment and the important implications of the process, the literature on the subject is very scarce. Mottershead et al. (2007, 2008) and Bruthans et al. (2008) measured erosion on salt outcrops in the Cardona diapir (NE Spain) and in various salt extrusion of the Zagros Mountains (Iran), respectively, using a limited number of short erosion pins, many of which were shifted out of the ground by rapid denudation and thus providing minimum estimates. Also at Cardona Diapir, Mottershead et al. (2008) quantified erosion in small outcrops comparing 3D surface models captured by a total station. De Waele et al. (2009, 2020) measured surface change with a Micro-Erosion Meter (MEM) on rock salt in the hyperarid Atacama Desert, but lacking rainfall control. The assessment of regional denudation rates in salt diapirs using discharge and solute flux data has been comprehensively addressed in the Konarsiah Diapir of the Zagros Mountains (Zarei et al., 2012) and Mount Sedom Diapir in Israel (Frumkin, 1994), where the salt is largely concealed by capsoil and caprock, respectively. Solutional denudation of

* Corresponding author.
E-mail addresses: guillermo.perezv@unizar.es (G. Pérez-Villar), fgutier@unizar.es (F. Gutiérrez).

https://doi.org/10.1016/j.geomorph.2026.110228
Received 27 October 2025; Received in revised form 11 February 2026; Accepted 13 February 2026
Available online 16 February 2026

rock salt has important practical implications, including the hydrochemical degradation of water resources (e.g., Zarei, 2016; Jalali et al., 2019), and modelling the long-term evolution of salt diapirs, increasingly targeted as geostorage sites (e.g., radioactive waste, hydrogen; Warren, 2016; Duffy et al., 2023). The development of the latter task is greatly hindered by the shortage of denudation data and the often misleading assessments of diapiric rise (e.g., Talbot et al., 2000; Gutiérrez et al., 2025b).

This work contributes to fill the significant knowledge gap related to surface denudation on rock salt by assessing erosion in a site at Cardona Diapir (NE Spain) with a broad diversity of karren features, using multiple methods (erosion pins, terrestrial laser scanner, ground-based SfM photogrammetry) in combination with a daily rainfall record. A number of studies illustrate the suitability of multi-temporal high-resolution 3D models captured by terrestrial laser scanner (TLS) or developed by Structure from Motion (SfM) Photogrammetry for assessing soil erosion (Nadal-Romero et al., 2015; Gulam et al., 2018; Mirzaee et al., 2024; Torra et al., 2025). The main objectives of this work include: (1) assessing surface denudation rates normalized to rainfall on a salt exposure; (2) exploring the role played by extrinsic and intrinsic factors on solutional denudation; (3) analyzing with high-resolution data the impact of karren microtopography on erosion variability; and (4) illustrating the use of erosion rates and diapiric-uplift rates to model the long-term geomorphic evolution of rising diapirs.

2. Geological and geomorphological setting

2.1. General setting of the Cardona Diapir

The actively rising Cardona salt extrusion occurs associated with the core of the NE-SW-oriented Cardona-Pinós Anticline, within the Ebro Cenozoic Basin in NE Spain (Fig. 1). This is a buckle anticline cored by the late Eocene Cardona Saline Formation, which is conformably overlain by a thick succession of alluvial mudstones and sandstones of the late Eocene-Oligocene Suria and Solsona formations (Riba et al., 1983; Sans and Verges, 1995; Sans, 2003). The marine Cardona Saline Formation, with an original thickness of 300–350 m, mainly consists of halite with a significant proportion of K—Mg chlorides (Pueyo, 1975; Riba et al., 1983; Rosell and Pueyo, 1997). In Late Quaternary times, entrenchment of the transverse SE-flowing Cardener River unroofed of the crest of the anticline, leading to the emergence of the salt (Pérez-Villar et al., 2024). The currently active salt rise in the diapir (passive salt wall) is driven by both differential overburden loading and erosional unloading related to greater supra-salt sediments at the adjacent synclines and on the valley margins, respectively (Pérez-Villar et al., 2024).

Long- and short-term rates of diapiric salt rise have been recently estimated using numerically dated uplifted deposits and DInSAR (Differential Interferometric Synthetic Aperture Radar) studies, respectively, yielding similar displacement rates and spatial patterns (e.g., greater uplift towards the salt wall axis, away from the frictional margins). Up-warped radiocarbon-dated Holocene terraces indicate uplift rates within the range 36.5–12.2 mm/yr (Pérez-Villar et al., 2024). DInSAR displacement data in salt outcrops indicate net vertical surface uplift related to the antagonistic effect of salt rise and surface salt dissolution, with values that reach 15 mm/yr in the Bofia Gran (Pérez-Villar et al., 2025a).

From the geomorphological perspective, the NE-SW oriented Cardona salt extrusion is 2 km long and 0.7 km wide, and covers an area of 0.9 km^2. In the SW sector, where the salt has been unroofed more recently (i.e., inmature diapiric landscape), the topography is featured by a dome-shaped hill 90 m in local relief (Salt Mountain) (Fig. 1). On the outer slopes of the hill the salt is mainly covered by upturned colluvial deposits (i.e., drape-folded flaps) derived for the surrounding outcrops of mudstones and sandstones (Suria and Solsona formations). The central sector of the Salt Mountain is carved by an enclosed karst depression 300 m long and 70 m deep (Bofia Gran). The steep slopes of this basin display salt outcrops with striking karrenfields and sectors where the salt is concealed by colluvium derived from the slope crest or clayey residual capsoils (i.e., in situ accumulation of dissolution residue (Lucha et al., 2008; Pérez-Villar et al., 2024). The Bofia Gran drains

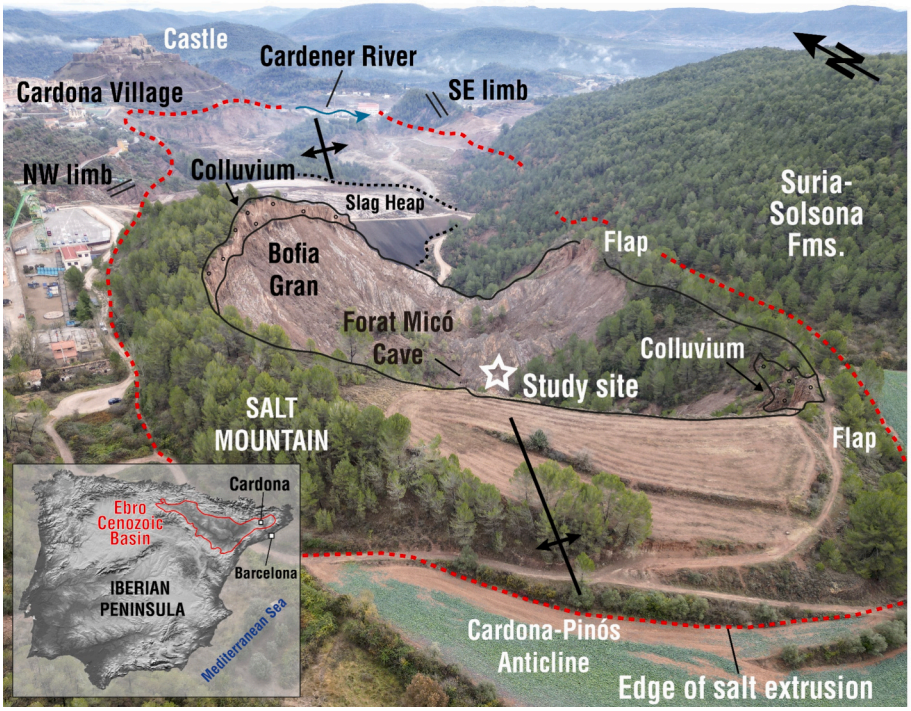

Fig. 1. General view of the active Cardona salt extrusion associated with the Cardona-Pinós Anticline and the transverse Cardener River valley. The study site (asterisk) is located in a large internally drained depression (Bofia Gran). This basin is carved in the dome-shaped Salt Mountain; which flanks are covered by upturned colluvial flaps. Inset relief model shows the situation of the Cardona Diapir in the NE sector of the Ebro Cenozoic Basin.

internally through a ponor, which corresponds to the upper entrance of the 640 m-long Forat Micó Cave (Cardona and Viver, 2002). The study site is located on salt slopes in the lower part of the Bofia Gran (Fig. 1). The area has a Mediterranean climate with an average annual precipitation of 508 mm and a mean annual temperature of 19 °C (Font-Soldevila, 2006).

2.2. The investigation site

The investigation site, covering approximately 50 m^2, is located in the axial sector of the Cardona salt wall (Fig. 1). Here, the Cardona Saline Formation consists of centimeter-thick halite beds interbedded with millimeter-thick clay partings (Figs. 2, 3). Halite represents ~93% of the rock exposure, while clay (7%) is mainly composed of illite (81%) and chlorite (19%) according to X-Ray Diffraction analysis (XRD). The structure is characterized by tight curtain folds with near-vertical axes, related to the radial contraction that experiences the salt when flows upward into a constriction (e.g., diapir stem) (Talbot and Jackson, 1987; Jackson and Hudec, 2017). The variable slope direction at the study site tends to be oriented perpendicularly to bedding. Consequently, runoff as well as the orientation and slope of the karren (i.e., flutes, bevels, runnels) tend to be oriented perpendicularly to stratification, cutting across bedding (Fig.2, 3A).

During dry periods the salt surface is partially covered by white fibrous halite efflorescences related to condensation-dissolution and evaporative re-precipitation (Fig. 3B). The salt efflorescences are readily dissolved and detached during rainfall events. The exposed clay interbeds typically display porous, bulbous masses of expended clay with

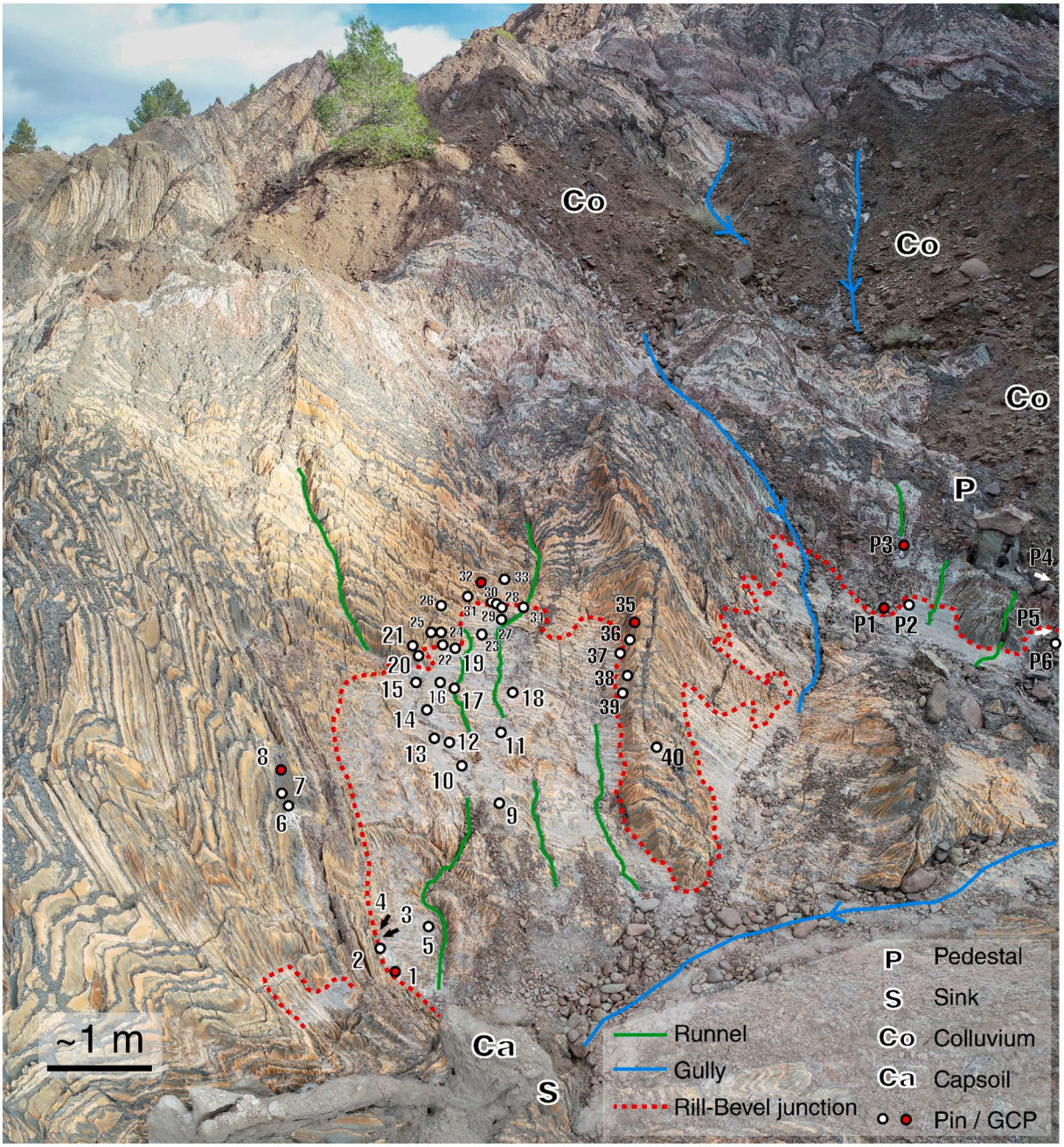

Fig. 2. Oblique view of the investigation site showing the distribution of erosion pins and ground control points, as well as the main geomorphic features developed on tightly folded salt with clay partings. The discontinuous red lines mark the junction between steep slopes dominated by solution flutes and more gentle areas carved by solution bevels. (For interpretation of the references to colour in this figure legend, the reader is referred to the web version of this article.)

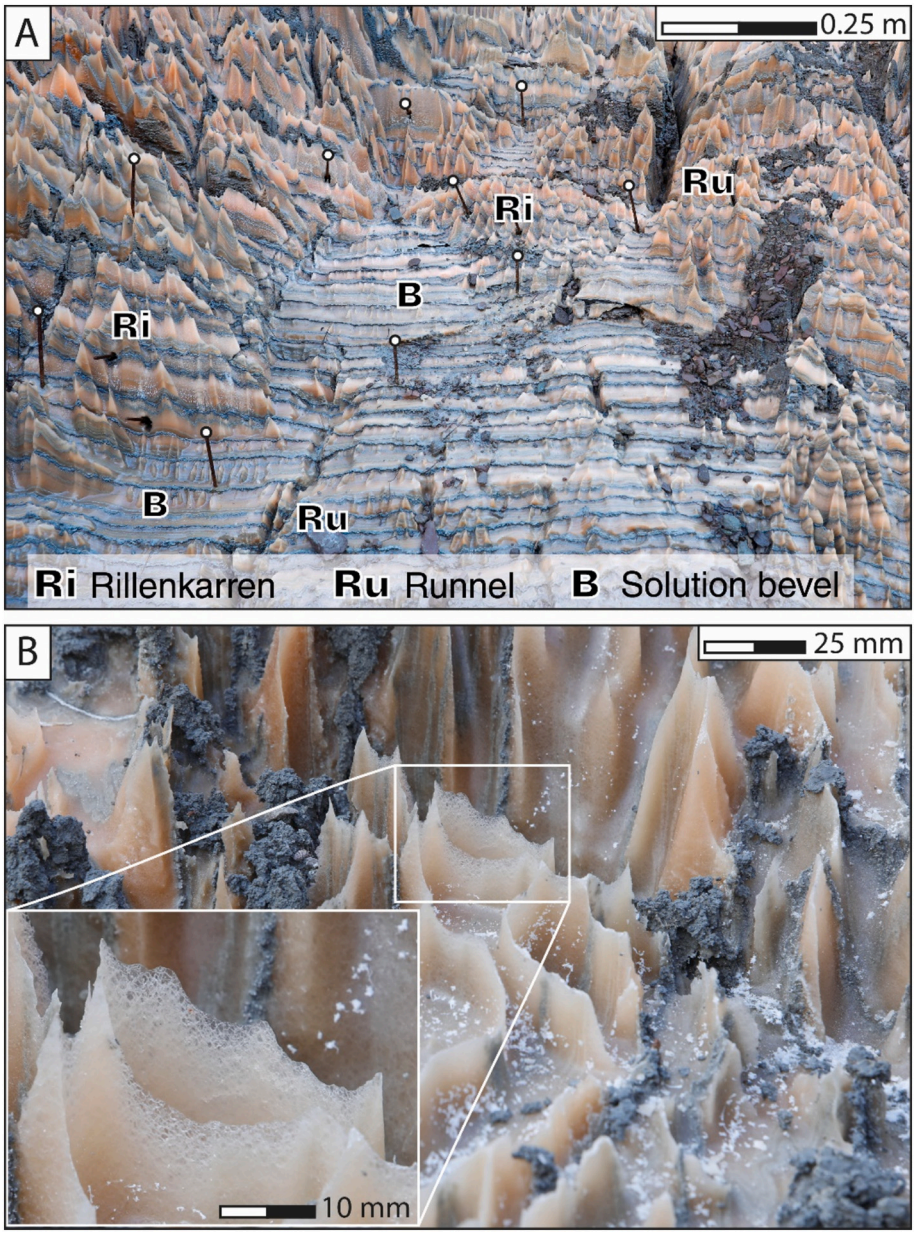

Fig. 3. Images showing some of weathering features and karren developed at the investigation site. A: Rock salt exposure sculptured by solution flutes, solution bevels and solution runnels. The upper tip of erosion pins is marked with a circle. Then photograph was taken on 14 December 2021, 320 days after the installation of the erosion pins and following a rainfall event that washed away saline efflorescences. B: Rillenkarren with razor-sharp ridges, expanded grey clay partings and white halite efflorescences. Close-up view in inset illustrates the extremely sharp (crystal thickness) ridges with combs and spikes flanking the solution flutes.

acicular gypsum crystals (Fig. 3B). The swelling of the clays, given the lack of expansive clay minerals (e.g., smectite), is ascribed to wetting and drying cycles, together with dissolution and re-precipitation of displacive gypsum crystals (Pérez-Villar et al., 2025b). Dissolution of halite leads to the in situ accumulation of residual clay in low-gradient areas, forming a protective "capsoil" (Bruthans et al., 2009; Gutiérrez et al., 2025a) (Fig. 2). Above the investigation site, salt slopes are partly covered by loose gravels derived from the rim of the Bofia Gran, capped by upturned colluvial flaps (Figs. 1, 2). Locally, large sandstone boulders protect the underlying salt from dissolution, promoting the development of pedestals (Karrentische; Bögli, 1961) (Fig. 2). The slope micromorphology is dominated by a karren assemblage comprising, in descending order (Ginés and Lundberg, 2009; De Waele and Gutiérrez, 2022) (Fig. 2, 3A): (1) solution pits (Rainpits) in low-gradient crests; (2) solution flutes (Rillenkarren) in the upper and steep slope sections; and (3) solution bevels (Ausgleichsflächen) in the lower and gentle slope sections. Both the rainpits and the solution flutes are flanked by razor-sharp ridges with crystal-scale thickness highly susceptible to dissolution erosion (i.e, high specific surface) (see inset in Fig. 3B). Additional features include solution runnels mainly carved in solution bevels, small gullies where runoff concentrates, and small cover-collapse sinkholes that may act as runoff and sediment sinks (Fig. 2). Detailed information on the morphometry and evolution of the salt karren at the study site can be found in Pérez-Villar et al. (2025b).

3. Methodology

Three techniques with variable spatial resolution and accuracy have been applied to quantitatively assess erosion in the salt exposures: (1) erosion pins; (2) Terrestrial Laser Scanner (TLS); and (3) ground-based Structure from Motion (SfM) Photogrammetry. Erosion pins were distributed in variable geomorphic settings, while TLS and SfM

Photogrammetry covered the total investigation site (ca. 50 m^2). Data from the Cardona meteorological station of the Servei Meteorològic de Catalunya (1.3 km from the outcrop), including daily precipitation, as well as mean daily temperature and relative humidity, were used to assess the role of rainfall and other factors on salt erosion (see monthly precipitation in Supplementary Data).

3.1. Erosion pins

A total of 40 erosion pins were placed in the salt bedrock oriented perpendicular to the rock surface by means of a drill and a hammer (Fig. 2). We used pointed stainless steel rods 0.4 m long and 6 mm in diameter driven around 0.35 m into the rock, remaining strongly fixed to the ground over the whole monitoring period. The distance between the upper tip of the erosion pins and the rock surface (D) was systematically measured on the upslope side of the pins using a digital caliper (Silverline Tools, range 300 mm, accuracy 0.01 mm). Variations of D provide values of surface-normal erosion (ΔD) (Fig. 4). A total of 11 measurement intervals were carried out between 28/01/2021, when the pins were installed, and 11/11/2023, spanning a total of 1017 days (ca. 2.8 yr.). The temporal spacing of the measurements varied between 15 and 191 days. The maximum ΔD reached 180 mm, and consequently none of the erosion pins were lost. Additional parameters were measured at each point, including the inclination of the pin with the horizontal on the outer side of the slope (I), the local gradient of the rock slope (S), and the 3D distance between the pin and the slope crest (L), providing an indirect estimate of the runoff contributing area (Fig. 4). The 40 erosion pins were distributed covering a wide range of topographic and geomorphic settings (Fig. 2): steep to nearly vertical non-dissected slopes (9); solution bevels (15); solution flutes (11); solution pits (3); and solution runnels (2). A few anomalous measurements were recorded related to factors such as accumulation of debris at the base of the pin, or abrupt surface changes at erosion pins located close to a ridge crest, when the crest was lowered below the pin (see inset in Fig. 4).

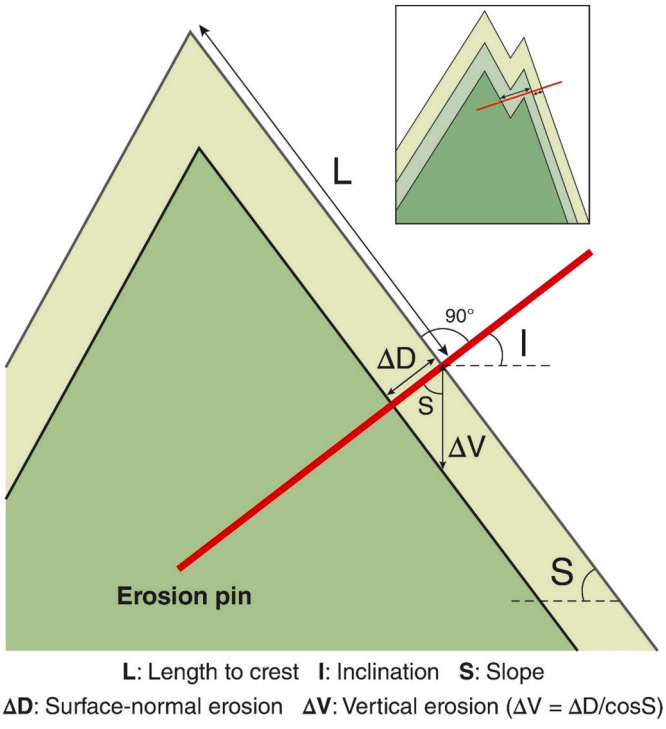

Fig. 4. Sketch illustrating the installation of erosion pins perpendicular to the local slope, and parameters measured. Note that vertical erosion (ΔV) tends to ∞ as the slope angle (S) approaches to 90° (cos 90 = 0). Inset figure shows anomalously high surface-normal erosion related to downwearing of a secondary ridge crest below the erosion pin.

3.2. Terrestrial laser scanner (TLS)

Terrestrial Laser Scanner (TLS) was used to generate 3D models of surface change comparing point clouds acquired at three different dates (21/05/2021; 20/06/2022; 16/12/2022), with a temporal spacing of 395 and 179 days, respectively, and covering a total time span of 1.57 years. A Faro Focus 3D X330 TLS was used in the two initial surveys and a Faro Focus Premium 350 in the last one. These devices have a detection range of 0.6–330 m, a ranging error of ±1 mm, and angular accuracies of 0.009° and 0.005°, respectively. Each survey comprised 10–11 partial and overlapping scans. Registered compound point clouds were generated merging the partial scans of each survey using the cloud-to-cloud tool of the SCENE software (©2024 FARO Technologies, Inc.). Common referencing of the point clouds was performed using the local coordinates of six black and white targets (see inset in Fig. 5) placed on erosion pins and extracted from the first compound point cloud. This approach implicitly assumes that the targets, that are not affected by erosion, remain stationary. Nonetheless, as revealed by geomorphic and DinSAR studies, the salt bedrock experiences continuous diapiric rise at rates of the order of cm/yr (Pérez-Villar et al., 2024, 2025a). However, as discussed below, this rock movement has limited impact on this work, since the displacement can be reasonably assumed as spatially uniform at the spatial and temporal scale of the investigation. Table 1 includes data on the date, time lapse, number of points, resolution, and error of the compound point clouds used to generate 3D models of surface change.

3.3. Structure from motion photogrammetry

Following the recommendations outlined in James et al. (2019), a series of high-resolution, close-range Structure-from-Motion (SfM) photogrammetric models were generated using oblique, overlapping photographs (.jpeg format). The images were acquired with a camera mounted on a tripod positioned between 1.5 and 5 m from the targeted rock surface. The photographic equipment consisted of a Canon EOS 5D Mark IV full-frame camera (30.4 MP CMOS sensor) with a Canon 16–35 mm f/4 L IS USM lens set at a constant focal length of 35 mm. To ensure optimal image quality in terms of sharpness and exposure, camera settings included a high aperture (f/8–11) for high depth of field, low ISO values (100−200) to minimize noise, and automatic shutter speed. Over a monitoring period of 715 days (1.96 years), five image acquisition campaigns were carried out on the following dates: 19/05/21, 14/12/21, 17/06/22, 31/11/22, and 04/05/23. A total of 38–73 photographs were taken in each survey, which were processed using Agisoft Metashape Professional 1.7.1© to generate 3D dense point clouds.

The models were referenced using four fixed targets mounted on erosion pins and the local coordinates extracted from the first terrestrial laser scanning (TLS) point cloud (Fig. 5). This approach allowed consistent referencing between the TLS and photogrammetric models. The resulting point clouds exhibit spatial resolutions ranging from 511 to 859 points/cm^2. The ground control point errors vary between 1.68 and 7.39 mm, with higher errors in the more recent datasets. This progressive error increase is likely due to slight displacements of the targets attributable to diapiric uplift and distortion of the erosion pins (e.g., corrosion, deformation). On average, the dense point clouds contain 269,316,022 points, with a mean density of 741 points/cm^2 and an average root mean square error (RMSE) for ground control point registration of 4.6 mm, as reported by Agisoft Metashape Professional©. Further details on each survey and the resulting 3D datasets are compiled in Table 2.

3.4. Comparison of 3D point clouds

The successive TLS and photogrammetric point clouds with common

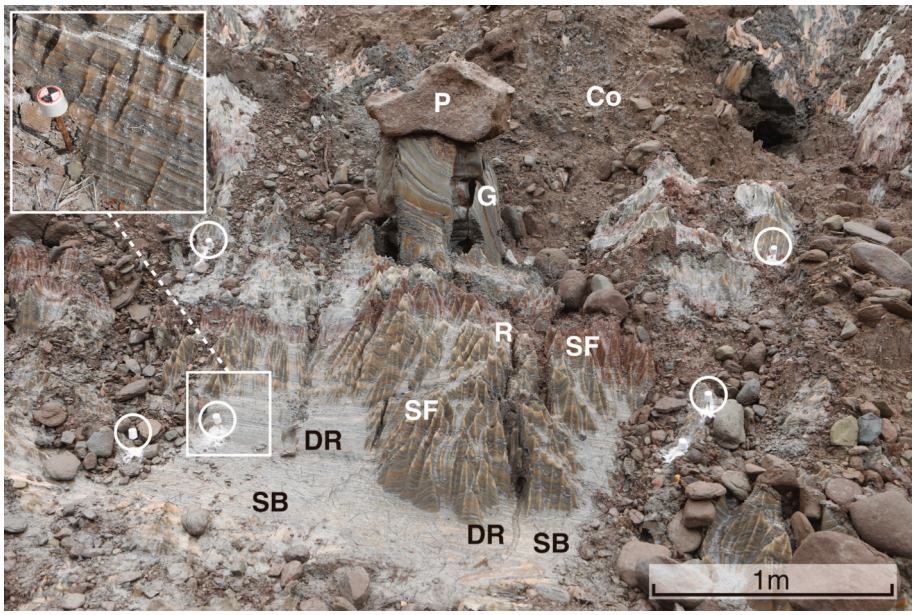

Fig. 5. Partial image of the investigation area (28/1/2021) illustrating the diversity of karren types and some ground control points (circles) installed on erosion pins. Close-up view of one ground control point in inset image. P: pedestal; G: grike; SF: solution flutes; R: runnel, DR: decantation runnel; SB: solution bevel; Co: colluvium.

Table 1
Data of the 3D point clouds captured by TLS. MPE stands for mean point error, which is the mean registration error of the compound point clouds.

Point cloud date	21/05/2021	20/06/2022	16/12/2022
Time lapse (days)	–	395	574
Number of points	87,125,730	64,180,189	106,559,689
Spatial resolution (points per cm^2)	89.9	66.2	109.9
MPE (mm)	12.1	11.9	10.6

registration were compared using the M3C2 algorithm (Lague et al., 2013) from the CloudCompare software in order to obtain 3D models of surface change. The M3C2 algorithm measures the mean 3D distance between two sets of point clouds considering the average position of the points within a surface-normal cylinder with a given diameter and depth. All the point clouds were filtered to remove undesired noise, such as persons or equipment. The photogrammetric point clouds, with extremely high resolution (500–1000 points/cm^2), were subsampled to 5 mm for the sake of acceptable processing times. Initially, the M3C2 algorithm was applied to a number of point clouds in standard mode, using an investigation depth of 0.5 m and multiple projection diameters (100, 50, 30, 10, 5 mm). These values refer to the height and diameter of the surface-normal cylinder, respectively. The comparison of the resulting 3D surface change models revealed a significant quality increase with projection diameters $\leq$30 mm, satisfactorily capturing spatial variations related to the very high roughness of the karren topography. Based on this assessment, a value of 10 mm was selected for the projection diameter and normal scale (used to determine the surface-normal direction), together with 0.5 m investigation depth, offering a good compromise between processing times and resolution. Additionally, the algorithm computes a local confidence interval that identifies statistically significant changes at a 95% confidence interval, taking into account the surface roughness of the clouds, their position uncertainty, and their registration error (Lague et al., 2013). It is important to note that the surface changes over the monitoring periods are dominated by centimeter-scale values, much higher than the millimeter-scale positioning errors associated with the TLS (Table 1) and photogrammetric (Table 2) point clouds.

4. Results

4.1. Erosion pins

The cumulative surface-normal erosion or accumulation (negative values) measured at the erosion pins over the whole monitoring period (1017 days; ca. 2.8 yr.), with a total precipitation of 1055 mm, ranges from 180.6 mm to −5.4 mm. The mean value recorded over this period is 96.9 mm. Mean annual surface-normal erosion/accumulation rates vary between 64.8 mm/yr and −1.9 mm/yr, with an average value of 34.8 mm/yr. Erosion/accumulation values per 100 mm precipitation measured in the different erosion pins show maximum, minimum and mean values of 17.1 mm, −0.5 mm, and 9.2 mm, respectively, the latter with a standard deviation of 5 mm. These data reveal significant variability in the surface-normal erosion under uniform meteorological conditions.

Table 3 compiles for the eleven measurement intervals maximum, minimum and average surface-normal erosion/accumulation (cumulative and normalized to 100 mm of precipitation) measured in the pins, together with the corresponding meteorological variables (precipitation, and averaged temperature and relative humidity). The potential

Table 2
Data of the photogrammetric 3D point clouds. RMSE: root mean square error of the ground control point registration.

Date	19/05/21	14/12/21	17/06/22	31/11/22	04/05/23	Mean
Time lapse (days)	–	209	185	63	154	137.5
Number of points	2.4E+08	2.9E+08	2.9E+08	2.4E+08	2.30E+08	2.64E+08
Spatial resolution (points per cm^2)	511	650	696	859	686	741
Control points RMSE (mm)	1.685	3.053	5.108	7.387	6.835	4.626

Table 3
Precipitation, mean temperature, and mean relative humidity recorded at the Cardona meteorological station over the eleven measurement intervals, and the corresponding maximum, minimum and average surface-normal erosion (or accumulation; negative) expressed as cumulative values and values normalized to 100 mm precipitation. Ppt: precipitation. ΔD: surface-normal erosion (or accumulation; negative). *This measurement interval starts from the data obtained on 23/9/2022 due to erroneous rainfall record in the period 24/8/2022–23/9/2022.

Measurement date	Ppt in last interval (mm)	Cumulative ppt (mm)	Daily averaged temperature (°C)	Daily averaged relative humidity (%)	Interval duration (days)	Max / min / mean ΔD (mm)	Max / min / mean ΔD normalized to 100 mm of precipitation
28/1/21	–	–	–	–	0	–	–
11/3/21	29.5	29.5	8.05	84.83	42	8.57 / 0.01 / 3.4	29.05 / 0.03 / 11.53
19/5/21	72.9	102.4	11.16	71.44	70	14.54 / 0.06 / 6.93	19.95 / 0.08 / 9.51
3/6/21	30.6	133	17.23	68.13	15	12.58 / -0.01 / 3.27	41.11 / -0.03 / 10.69
11/8/21	68.1	201.1	22.09	62.76	69	20.41 / -0.5 / 4.06	29.97 / -0.73 / 5.96
26/10/21	137.6	338.7	18.45	75.52	76	103.07 / -1.99 / 12.15	74.91 / -1.45 / 8.83
14/12/21	57	395.7	6.81	82.76	49	20.11 / 0.1 / 6.44	35.28 / 0.18 / 11.30
17/6/22	157.5	553.2	10.14	72.18	185	50.13 / 0.17 / 16.8	31.83 / 0.11 / 10.67
24/8/22	126	679.2	24.29	61.09	68	24.32 / -4.68 / 11.27	19.30 / -3.71 / 8.94
29/11/22*	49.1	728.3	13.59	78.39	67	10.89 / -15.01 / 2.04	22.18 / -30.17 / 4.15
04/5/23	104.9	833.2	7.50	74.84	156	42.82 / -6.46 / 9.59	40.82 / -6.16 / 9.14
11/11/23	221.7	1054.9	20	68.94	191	86.54 / -4.68 / 20.32	39.03 / -2.11 / 9.17

control exerted by the meteorological variables on solutional erosion was explored. As expected, the relationship between average erosion in each measurement interval and both temperature and relative humidity show very low coefficients of determination (R^2) of 0.048 (*p*-value = 0.472) and 0.07 (p-value = 0.382), respectively. The relationship between erosion and precipitation (P) has been analyzed considering all the surface-normal erosion measurements after removing negative values (aggradation; 35 out of 440), and the means calculated for each interval. The linear regression between precipitation and the 11 average erosion values (ΔD = 0.0954P-0.3387) shows a high correlation, with a coefficient of determination (R^2) of 0.95 (p-value ≤0.00001) (Fig. 6). The slope of the best-fit curve suggests an average erosion of 9.5 mm per 100 mm of rainfall. In contrast, the relationship between precipitation and the 405 erosion measurements (ΔD = 0.0954P-0.3387) shows a poor correlation (R^2 = 0.29; p-value ≤0.00001) (inset in Fig. 6), indicating that other factors in addition to rainfall, such as slope angle, micro-topography (i.e., karren type), or distance to the crest or divide (i.e., proxy for runoff contributing area) may play an important role.

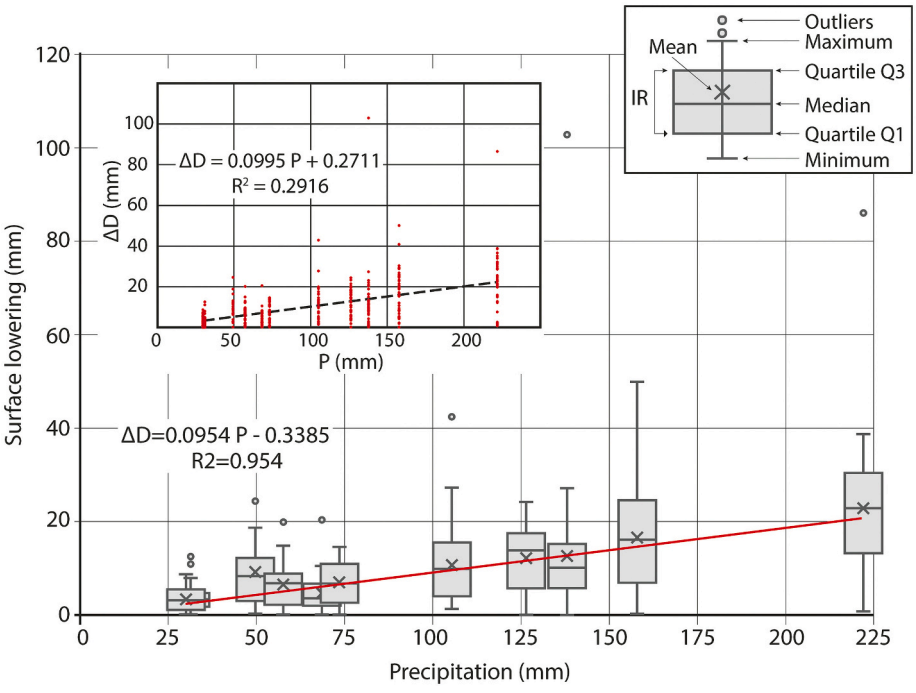

Fig. 6. Graphs showing the relationship between precipitation and erosion measured in the different intervals, represented as boxplots and as all values (inset). The regressions have been generated with the means of each interval (lower graph) and all values (inset).

The graph in Fig. 7A plots erosion measured in the pins, normalized to 100 mm precipitation and classified according to the karren type, versus slope angle. Note that karren shows a zonation controlled by the gradient of the slope (Pérez-Villar et al., 2025b) (Fig. 7A): solution pits (0°), solution bevels (6–34°), runnels (20–49°), solution flutes (35–82°), steep walls (65–92°). The erosion values (normalized to 100 mm of precipitation; ΔD_{100}) decrease as the slope (S) increases, showing are fairly good linear correlation ($\Delta D_{100} = -0.1358S + 15.032$; $R^2 = 0.6794$; *p*-value <0.001). The slope of the best-fit curve suggests an average increase of around 2.7 mm in ΔD_{100} per 20° decrease in the slope angle. In contrast, the graph that plots erosion (ΔD_{100}) versus distance to the divide (L), as a proxy for the runoff contributing area, shows no correlation ($\Delta D_{100} = 0.0058\ L + 7.7301$; $R^2 = 0.0012$; p-value = 0.8276) (Fig. 7B). Poor correlation is also obtained with the regressions derived from specific karren types (e.g., bevels) or karren assemblages (solution flutes and bevels).

4.2. SfM photogrammetry and terrestrial laser scanner

Models of surface-normal change have been produced carrying out M3C2 comparisons with the multi-temporal photogrammetric and TLS point clouds. The first point cloud was compared with successive point clouds of each technique, providing spatially distributed measurements

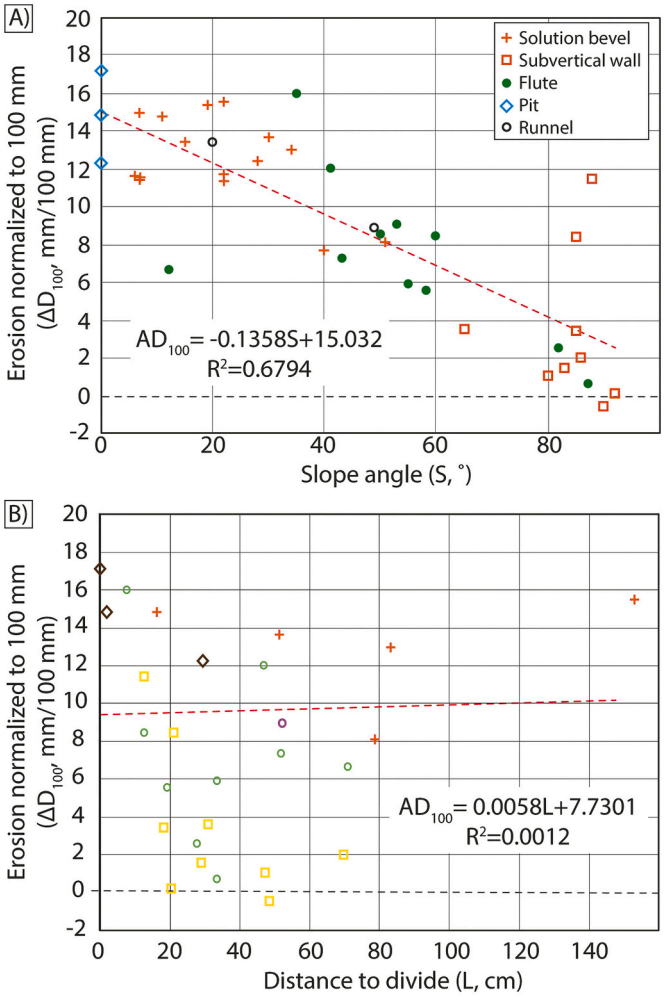

Fig. 7. Graphs showing the relationship between the erosion measured in the erosion pins, normalized to 100 mm precipitation, and the variables slope angle (A) and distance to the divide (B). The points are classified according to the karren type. Regression curves and equations, together with the coefficients of determination, are indicated.

of cumulative surface-normal erosion for different time lapses (209, 394, 560 and 715 days for photogrammetry; 395 and 715 days for TLS) (Fig. 8A-F). The comparisons were performed applying 10 mm of projection diameter, and the resulting models have spatial resolutions of 4 points/cm^2 and 89 points/cm^2 for the photogrammetric- and TLS-derived models, respectively. Note that the photogrammetric point clouds were subsampled at 5 mm, while full-resolution was retained in the TLS points clouds. Pérez-Villar et al. (2025b) illustrate the use of higher-resolution comparisons using photogrammetric point clouds, which allowed the detailed evolutionary analysis of individual karren features.

The average, median and mode values of surface-normal erosion normalized to 100 mm precipitation measured in the multiple comparisons show consistency among the different intervals and techniques (Table 4). Average erosion values normalized to 100 mm precipitation range between 8.2 and 10.1 mm. The average values obtained with point clouds from different methods but covering almost coincident time intervals are very similar; 9.6 and 9.4 mm for photogrammetry versus 10.1 and 9.5 mm for TSL, respectively (see columns with the same grey tone in Table 4). The data obtained by these techniques, in agreement those from the erosion pins, indicate an overall surface-normal erosion rate of around 10 mm per 100 mm rainfall.

The multiple high-resolution surface-normal erosion models derived from photogrammetric and TLS data show the following main general features (Fig. 8A-F): (1) complex spatial patterns of erosion associated with the intricate microtopography and nature of the area (e.g., karren diversity, exposed versus concealed rock salt); (2) spatial consistency across time intervals and data source (photogrammetry versus TLS); (3) major control exerted by karren type and topography on erosion, with relatively high values in crests, low-gradient areas (bevels) and runoff concentration zones (runnels; see arrowhead in Fig. 8A-F), relatively low values on steep slopes, and null or negligible erosion in soil-covered areas.

Fig. 8G shows normalized frequency curves representing the proportion of points versus surface-normal erosion for each M3C2 model. As expected, the successive graphs from each technique are displaced towards the right (higher cumulative erosion) for models covering progressively longer intervals. The four frequency curves of the photogrammetric erosion models, covering a broader time span, show two phases: (1) from the first to the third, curve widening and flattening, indicating an increasing range of erosion values; and (2) from the third to the fourth very similar curve geometry, suggesting the surpassing of a time threshold from which most of the variability is captured by the data.

In order to compare solutional erosion in different karren types, erosion values corresponding to rillenkarren, bevels and runnels have been extracted from the photogrammetry-derived M3C2 model covering 394 days (19/05/21–17/06/22). Fig. 9 shows, for each karren type, frequency curves representing proportion of points versus erosion normalized to 100 mm. The rillenkarren graph in green (platykurtic) peaks at around 13 mm and reflects a wide range of erosion values, as expected for this karren type, comprising smooth flutes and razor-sharp ridges. The more pointed runnel curve in red (leptokurtic) also peaks at around 13 mm and shows a wide range of erosion values, but a great part of them concentrate around the mode (10–15 mm). The graph of the bevels in blue, with a simple planar morphology, display a much narrower range and peak around 11 mm. The whole area curve, covering all the geomorphic diversity and including soil-covered areas, peaks at around 13 mm and shows an asymmetric distribution, with greater proportion of points < 13 mm.

A comparison between the photogrammetric and TLS point clouds, as well as the derived erosion values, is illustrated in Fig. 10 using sections across a rillenkarren-bevel juntion and representing surface change over coincident time intervals. This example illustrates the tight consistency among the data obtained by both techniques. The lower resolution of the erosion data measured with the photogrammetric point

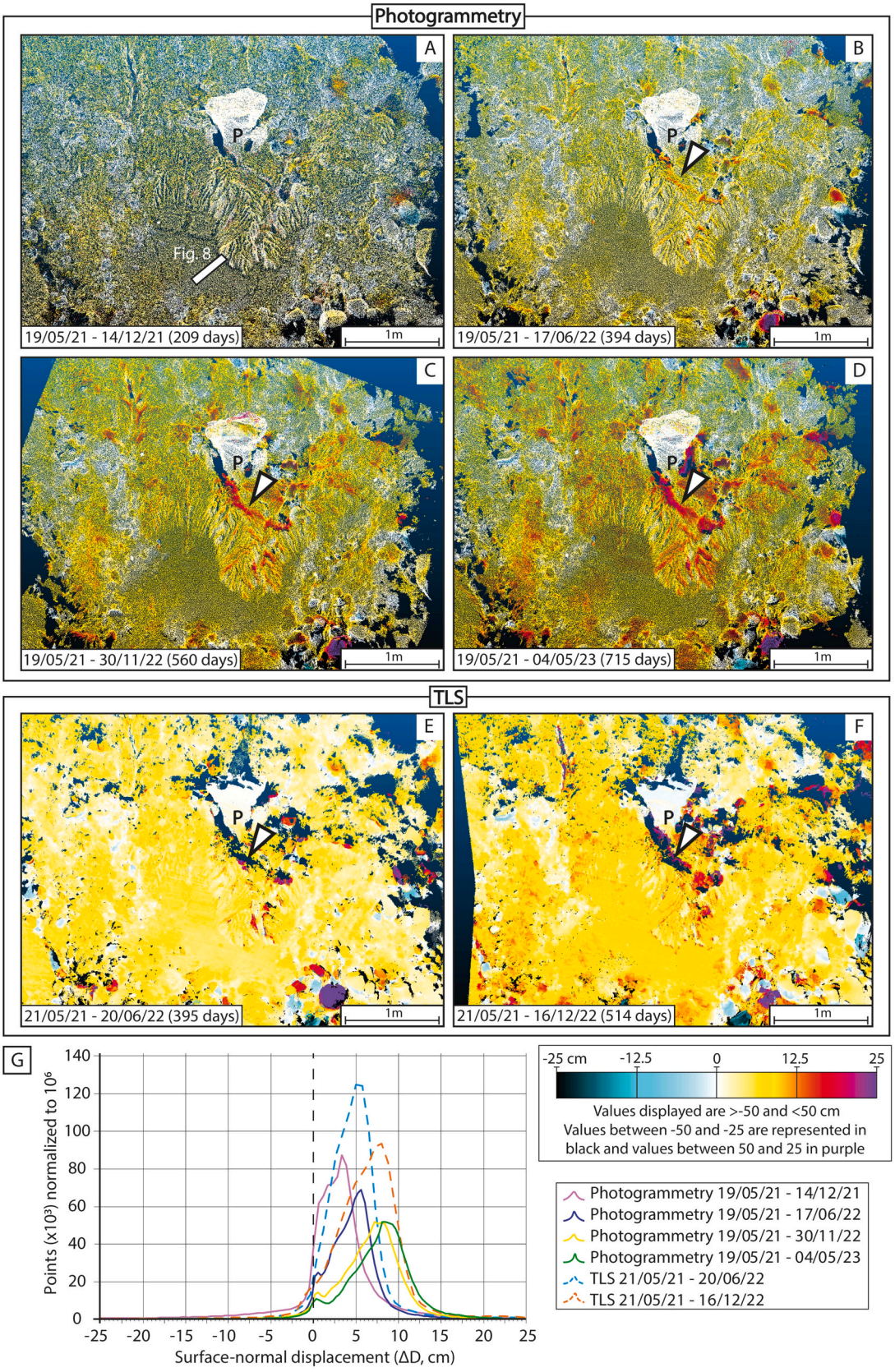

Fig. 8. Slope-normal surface change M3C2 models generated comparing multi-temporal photogrammetric (A to D) and TLS (E and F) point clouds. The models show cumulative changes occurred between the first acquisition and the successive ones. P stands for pedestal. White arrowhead points to area with faster erosion related to concentrated runoff. G: Frequency curves depicting proportion of points (normalized to 10^6) versus surface-normal displacement for each M3C2 model.

Table 4
Values of surface-normal erosion (mean, median, mode) and values normalized to 100 mm precipitation for the different M3C2 comparisons using TLS- and photogrammetry-derived point clouds. The grey tones indicate comparisons covering quasi-identical time intervals. Skewness and kurtosis of frequency curves shown in Fig. 8G are indicated. IQR: interquartile range.

	TLS		SfM Photogrammetry			
Time interval	21/05/21–20/06/22	21/05/21–16/12/22	19/05/21–14/12/21	19/05/21–17/06/22	19/05/21–30/11/22	19/05/21–04/05/23
Interval (days/years)	395 / 1.08	574 / 1.57	209 / 0.57	394 / 1.08	560 / 1.53	715 / 1.96
Precipitation (mm)	450.8	729.6	293.5	450.8	686.6	791.3
Mean erosion (mm)	45.4	69.5	24.1	43.3	64.3	75.4
Mean erosion normalized to 100 mm (mm)	10.1	9.5	8.2	9.6	9.4	9.5
Median (mm)	41.1	67.4	29.2	52.3	68.4	83.4
Median normalized to 100 mm (mm)	10.2	11.5	10.5	12	10.2	10.5
Mode (mm)	45.9	83.8	30.7	54.3	70.1	83
Mode normalized to 100 mm (mm)	9.1	9.2	10	11.6	10	10.5
IQR	42.6	44.7	34.0	39.7	41.5	48.9
Skewness	−0.26	−0.10	0.20	0.68	0.26	0.51
Kurtosis	29.26	18.49	16.59	22.84	15.67	14.82

clouds is not related to their original resolution, but to the down-sampling (5 mm) carried out for the M3C2 comparison (Fig. 10C). In agreement with the evolutionary patterns documented for salt karren in Pérez-Villar et al. (2025b), the time-lapse profiles show greater erosion in the low-gradient solution bevel that experiences near surface-parallel erosion. Moreover, progressive recession is observed at the abrupt rillenkarren-bevel junction.

5. Discussion

5.1. Comparison with other data

The number of previous studies providing direct measurements of erosion on rock salt exposures is very scarce. The techniques employed include erosion pins, micro-erosion meters (MEM), and comparison of digital surface models captured with a total station. Overall, the erosion measurements presented in those works compare well with our data, although suffer from a number of limitations, including: (1) exiguous number of point data; (2) limited geomorphic and slope-gradient coverage; (3) short monitoring period and/or meagre number of measurement campaigns; and (4) lack or poor rainfall data.

In Cardona, Mottershead et al. (2007) measured erosion using brass pins 50 mm long placed at three sites: (1) salt rock-fall blocks with surfaces sloping from 0 to 60°; (2) the steep (≥70°) sidewall of a bedrock collapse sinkhole carved by solution flutes; and (3) a single trittkarren (i.e., stepkarren). A significant number of the pins were lost by erosion, remaining only in the rockfalls ($n = 7$) and the sinkhole wall ($n = 16$), where the measurement period extended over 244 and 496 days, respectively. Slope-normal erosion standardized to 100 mm precipitation ranged from 2.22 to 22.24 mm, with a mean of 12.26 mm, similar to our average values (Table 3). They observed a good reverse correlation between surface-normal erosion rate normalized to 100 mm and slope gradient, modeled by a linear function ($\Delta D_{100} = -0.20360S + 22.0156$; $R^2 = 0.864$) and a second order polynomial function ($\Delta D_{100} = -0.00248S^2 + 0.0238S + 19.285$; $R^2 = 0.906$). Their linear regression shows fairly higher slope than ours, with higher erosion values for low-gradient areas. In a subsequent study at Cardona, Mottershead et al. (2008) assessed erosion using a total station at site 2 (sinkhole sidewall) and site 3 (trittkarren), as well as at two additional sites in a salt-rich slag heap. They compared digital surface models 239 days apart with a resolution of 10–20 mm and co-registered using fixed ground control points, obtaining a weighted mean slope-normal erosion normalized to 100 m of 11.05 mm, aligned with our results (Table 3). The authors acknowledged that the resolution of the models was insufficient to capture the variability associated with the rugged micro-topography of the karren assemblages.

Bruthans et al. (2008) measured erosion at emergent salt diapirs in the Zagros Mountains of Iran, including salt extrusions in coastal areas (Hormuz, Namakdan; ca. 170 mm/yr) and in a higher elevation and more humid inland zone (Jahani; ca. 550 mm/yr). Erosion was

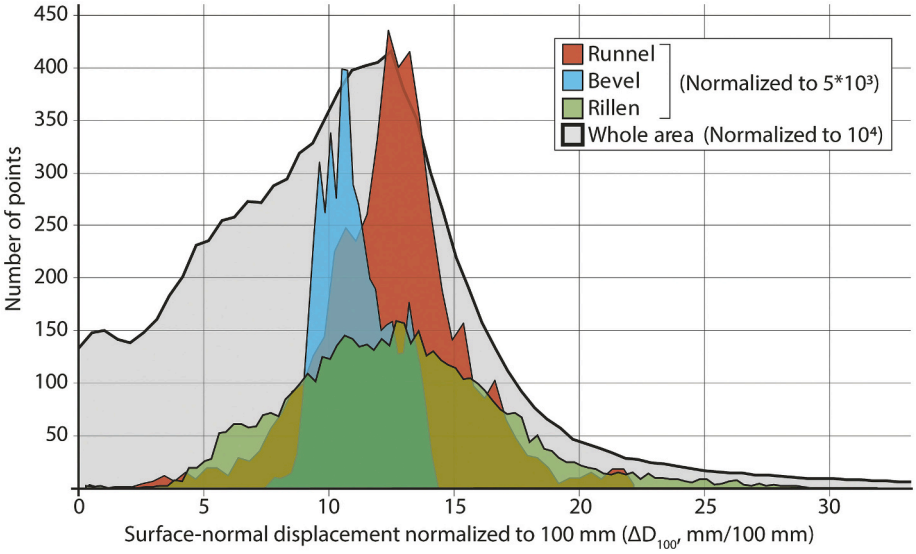

Fig. 9. Frequency curves showing normalized number of points (whole area: normalized to 10^4; specific karren types: normalized to $5*10^3$) versus surface-normal displacement normalized to 100 mm precipitation from M3C2 models obtained comparing two photogrammetric point clouds (19/05/21 and 17/06/22).

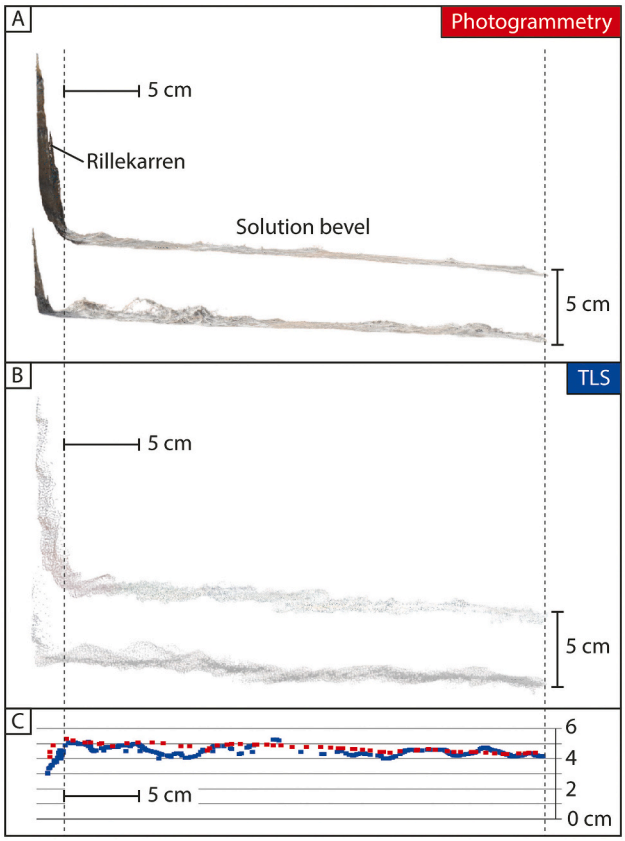

Fig. 10. A, B: Time-lapse sections across a rillenkarren-bevel junction (see location in Fig. 8A) constructed from photogrammetric and TLS point clouds. These sections are vertical slices extracted from the 3D point clouds, covering quasi-coincident time intervals (Photogrammetry: 21/05/21–20/06/22; 395 days, and TLS: 19/05/21–17/06/22; 394 days) and equal cumulative precipitation (450.8 mm). C: Graph representing surface-normal erosion measured along the photogrammetric (red) and TLS (blue) profiles. The lower spatial resolution of the photogrammetric-derived erosion values is related to the downsampling of the point clouds carried out before the M3C2 comparison. (For interpretation of the references to colour in this figure legend, the reader is referred to the web version of this article.)

measured using 32 erosion pins 110 mm long installed in 2000 and 2004, and measured once after four and one years, respectively. A significant proportion of the pins (16 out of 32) were unseated by erosion, providing minimum erosion values. The distribution of the pins was mainly concentrated on steep slopes (19 in slopes ≥60°), mainly corresponding to rillenkarren (20 out of 32). The data obtained at the 16 pins that persisted indicate an average vertical erosion rate normalized to 100 mm of 22.7 mm, using rainfall from distant stations. This high value is partially biased by the high slope of the measurement points and probably the scarcity of data. The average surface-normal erosion normalized to 100 mm and considering the slope values can be estimated at 6.3 mm, which is considerably lower than our average value.

In the Cordillera de la Sal, Atacama Desert, Chile, De Waele et al. (2009, 2020) measured erosion using a micro-erosion metre on rocksalt surfaces; 3 stations on horizontal surfaces and 2 on vertical surfaces. The measurements, covering intervals ranging between 127 and 1457 days, yielded annual erosion rates of 0.4 and 1.73 mm/yr for the vertical surfaces and an average of 0.80 mm/yr for the horizontal surfaces. The lack of rainfall control in this area with exiguous (≤20 mm/yr) and erratic precipitation precludes estimating normalized erosion values and making comparisons with our data.

5.2. Comparison between techniques

The erosion measurements obtained with the three techniques show a tight consistency. A comparison is presented in Table 6, indicating the slope-normal erosion normalized to 100 mm of precipitation at six erosion pins located within the area covered by photogrammetry and TLS. The average erosion values measured at these points show differences among techniques of 3.86% (photogrammetry vs. TLS), 3.35% (TLS vs. erosion pins) and 0.52% (photogrammetry-erosion pins). Differences among erosion measurements obtained using SfM, TLS, and erosion pins were assessed using the Friedman test. No significant differences were observed among the three techniques ($\chi^2 = 1$, df = 2, $p = 0.607$), suggesting that the methods provide comparable results at the sampled points. Although the number of common points was limited ($n = 6$), the consistency of measurements across points supports the reliability of the methods in this study. The close match between the erosion data obtained by photogrammetry and TLS is also illustrated in Fig. 10 depicting time-lapse sections of a rillenkarren-bevel karren assemblage and the resulting comparison. The coincidence among the results obtained by the different methods serves as an independent validation to assure the reliability of the approaches and results.

Erosion pins, which provide point data, do not allow resolving the small-scale spatial variability of erosion controlled by the complex karren micro-topography (e.g., faster erosion at sharp rillenkarren ridges). Nonetheless, this inexpensive, easy-to-implement, and fast approach allows capturing satisfactorily the variability related to some of the main controls, such as rainfall and slope gradient (Fig. 6, 7A). The difficulty faced in some previous investigations related to the prompt loss of short pins (50–110 mm long; Mottershead et al., 2007; Bruthans et al., 2008) can be easily overcome by installing longer pins. Considering that 100 mm rainfall leads to an average slope-normal erosion of around 10 mm, the 0.5 m long stainless steel pins used in this work could persist around 10 and 25 years in Cardona and the coastal salt extrusions of the Zagros Mountains, with mean annual precipitation of approximately 500 mm/yr and 200 mm/yr, respectively.

Both TLS and ground-based photogrammetry provide the means of generating co-registered multi-temporal point clouds with extremely high resolution (Tables 1, 2). The comparison of these point clouds allows accurately resolving the complex spatio-temporal evolution of karren (Pérez-Villar et al., 2025b) and the variability of the erosion associated with the high-roughness karren micro-topography. A factor that may constrain the working resolution of both approaches may be related to the computational capability of the hardware and software employed.

The main advantages of the ground-based photogrammetry with respect to TLS are: (1) the much lower cost (i.e., conventional camera versus TLS); (2) the simpler data acquisition process; and (3) the more even distribution of the points of the clouds, that tends to be biased in the case of TLS by the reflectance properties of the surface (exposed versus concealed salt). TLS may be a more suitable technique for investigating relatively large areas, although there is also the option of rapidly taking images over large areas using UAVs (Unmanned Aerial Vehicles), but with lower resolution.

Table 6
Slope-normal erosion normalized to 100 mm of precipitation (calculated using the longest interval for each technique), at six points by erosion pins, photogrammetry and TLS.

Selected pins	Photogrammetry (mm)	TLS (mm)	Pins (mm)
P1	5.26	5.80	6.01
P2	12.20	12.24	12.15
P3	10.08	9.08	10.24
P4	6.54	5.77	6.07
P5	11.66	10.70	11.70
P6	10.89	10.85	10.15
Average	9.44	9.07	9.39

5.3. Controls on solutional erosion and geomorphic implications

Measuring solutional denudation by direct short-term methods (e.g., standard tables, micro-erosion meter; Turowski and Cook, 2017) on bare surfaces underlain by carbonate rocks and gypsum is a challenging task because of the slowness of the dissolution process. Direct measurements of chemical erosion in these settings typically suffer from limited spatial and temporal representativeness, as well as reduced reliability, as much as the error margins tend to be close to the obtained erosion values (see review in De Waele and Gutiérrez, 2022). In contrast, as illustrated in this work, representative and reliable erosion measurements can be obtained in salt outcrops over short periods of time, thanks to the high solubility of halite (356,15 g/kg; grams of solute in 1 kg of solvent) and its rapid diffusion-controlled, first order kinetics (i.e., linear relationship between dissolution rate and saturation ratio) (Alkattan et al., 1997). Surface solutional erosion has greater geomorphic impact in salt outcrops than in exposures carbonate rocks, not only because the much more rapid halite dissolution, but also because infiltration tends to be much lower in salt formations, characterized by lower permeability and limited epikarst development (De Waele and Gutiérrez, 2022).

The consistent erosion data obtained by erosion pins, photogrammetry and TLS, with adequate spatial-temporal resolution, covering broad geomorphic diversity (i.e., karren types), and accompanied by daily rainfall data, provides insights into the role played by several factors on chemical erosion. Obviously, the amount of rainfall is the main factor that controls surface-normal erosion on salt outcrops (Fig. 6). The surface-normal erosion caused by 100 mm rainfall (ΔD_{100}) is around 10 mm on average, and may reach more than 20 mm (Fig. 6). The linear regression generated between average surface-normal erosion and precipitation ($\Delta D = 0.0954P\text{-}0.3387$; $R^2 = 0.95$) can be used to estimate the expected mean annual erosion rate in salt outcrops under different morphoclimatic environments. For instance, 9.2 mm, 23.5 mm, and 47.4 mm mean annual erosion for 100 mm, 250 mm, 500 mm annual precipitation, respectively. This relationship has relevant implications for understanding the geomorphic evolution of diapiric salt extrusions under different environmental conditions, where the share of salt exposures versus protecting residual capsoils can be highly variable (Bruthans et al., 2008, 2009; Gutiérrez et al., 2025a).

Slope gradient, as indicated in previous works (Mottershead et al., 2007, 2008; Bruthans et al., 2008), also plays an important role in slope-normal erosion, with increasing values as the slope declines. This trend is related to the fact that as the slope decreases, the rainfall water interacts with a comparatively smaller surface. This relationship aligns with the widely accepted interpretation whereby erosion in rillenkarren, which is the dominant karren type on salt slopes, is mainly related to direct dissolution caused by impinging raindrops with sufficient kinetic energy to penetrate the boundary layer (Glew and Ford, 1980; Ginés and Lundberg, 2009; Lundberg and Ginés, 2009). The linear regression generated between surface-normal erosion normalized to 100 mm rainfall and slope ($\Delta D_{100} = -0.1358S + 15.032$; $R^2 = 0.6794$) indicates an increase in ΔD_{100} of around 2.7 mm per 20° slope decline (Fig. 7A). Average ΔD_{100} values of around 4 mm, 7 mm, and 12 mm can be expected for 80°, 60°, and 20° slopes, respectively. Note that in a planar surface, the surface of salt exposed to rainfall is approximately 6 times greater in an 80° slope than in a 20° slope with the same planimetric area.

The erosion-slope relationship can be used as a tool to understand and predict quantitatively geomorphic evolution on salt outcrops. As an example, Fig. 11 illustrates the theoretical geomorphic evolution of a depression (or trough) with segmented slope profiles on rock salt exposures that steepen towards the margins. The stepwise evolutionary model depicts the surface-normal erosion experienced by the slopes and floor of the depression caused by 100 mm and additional 500 mm rainfall according to our linear erosion-slope regression. The effects of the decrease in the slope-normal erosion with slope steepening include: (1) more rapid deepening than widening of the depression; (2) overall slope steepening; (3) shortening or disappearance of the low-gradient slope segments and lengthening in the rest; and (4) progressive transformation in the overall 3D morphology from bowl- to more conical-shaped. The diagram also illustrates the increase in the deviation between slope-normal erosion and vertical erosion with the gradient (figures rounded to the first decimal). Obviously, the actual evolution of

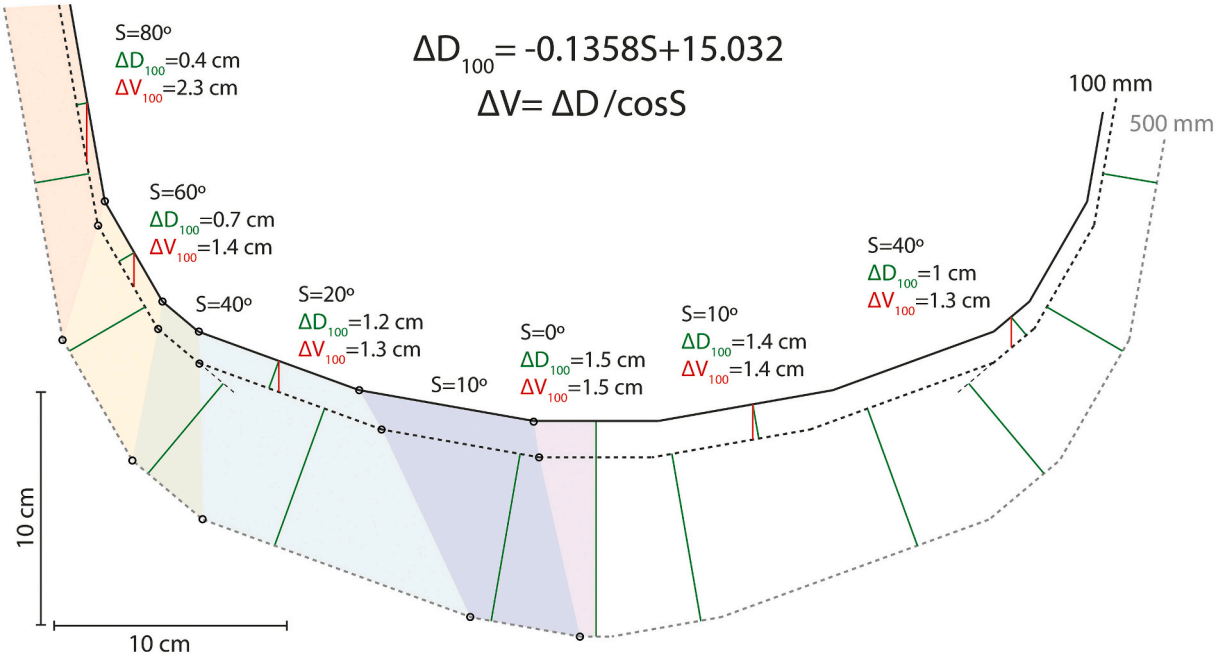

Fig. 11. Theoretical evolution of a depression with segmented slope profiles on salt using the obtained erosion-slope linear regression and considering a two-steps of erosion related to 100 mm and additional 500 mm rainfall. The slope segments are delimited on the left side with circles and colors. Green and red lines indicate surface-normal and vertical denudation, respectively. Numerical values refer to 100 mm rainfall. (For interpretation of the references to colour in this figure legend, the reader is referred to the web version of this article.)

specific depressions on salt may be significantly different, since other processes in addition to dissolution can operate. For instance, clay rich dissolution residue may accumulate in the floor of the basin, preventing its deepening and favoring its lateral enlargement.

The high-resolution surface change models (M3C2 comparisons) derived from photogrammetric and TLS point clouds reveal the strong control exerted by karren microtopography on erosion, resulting in significant variability across centimeter-scale distances (Fig. 8G). The lowest heterogeneity is observed in solution bevels (Fig. 9), where erosion values with a frequency peak at $\Delta D_{100} = 11$ mm show a limited range (7–14 mm), as expected for planar surfaces with regular slope and low roughness. A much wider range is observed in solution flutes (0–30 mm) and runnels (0–22 mm) with frequency peaks at $\Delta D_{100} = 13$ mm, where a whole range of slopes and microtopography occurs (e.g., sharp ridges versus smooth troughs). These data are in agreement with the complex and rapid spatial-temporal evolutionary patterns documented at Cardona using multi-temporal photogrammetric models (Pérez-Villar et al., 2025b). Rillenkarren show cycles of flute coalescence and splitting. Greater dissolution in the bottom of the flutes leads to progressively slimmer intervening ridges with very high surface/volume ratio, that are rapidly eroded, resulting in flute coalescence. Subsequently, broad flutes split by the development of nested incision. Rainpits are ephemeral karren that form, grow and lose their enclosed status very rapidly. Solution-bevels experience uniform slope-normal lowering accompanied by the backward retreat of its upper edge, at the rillenkarren-bevel junction. Pedestals can grow vertically at rates as high as 50 mm/yr by rapid erosional lowering of the slopes surrounding the stem (Pérez-Villar et al., 2025b).

Erosion rates measured in this study can be used to roughly estimate the volume of salt removed by surface erosion from the Bofia Gran enclosed depression (76,583 m^2 planimetric area), and compare it with the volume of salt restored by diapiric rise. According to our detailed mapping, salt exposures in the Bofia Gran cover 9814 m^2 (12.8%) and have an average topographic gradient of 40°. Our erosion versus slope regression derived from erosion pin data (Fig. 7A) indicates an average surface-normal erosion rate normalized to 100 mm (AD_{100}) of 9.6 mm for that slope. This value corresponds to a mean annual vertical erosion (AV = AD/cosS) of 63.5 mm considering an average annual rainfall of 508 mm and the estimated slope. The mean annual vertical erosion rate multiplied by the area of the salt outcrops yields a volume of salt of 623.2 m^3, which should be considered as a minimum value, since dissolution can also occur in rock salt covered by residual capsoils and slope deposits. The volume of salt restored by diapiric rise can be estimated at 1532–2680 m^3, considering the area of the Bofia Gran (76,583 m^2) and a range of uplift rates of 20–35 mm/yr constrained by DInSAR data and using numerically dated uplifted Holocene terraces (Pérez-Villar et al., 2024, 2025a). The overall higher contribution of diapiric rise is consistent with the geomorphic setting as revealed by the following lines of evidence: (1) the floor of the deep and internally drained Bofia Gran is perched around 40 m above the adjacent base level; and (2) the 640 m long Forat Micó Cave, which upper entrance is located in the bottom of the Bofia Gran (Cardona and Viver, 2002), is a rapidly incising sinuous and steep canyon with multiple-tiered notches unable to counterbalance diapiric uplift.

6. Conclusions

Previous works dealing with the assessment of erosion on rock salt exposures are very scarce and suffer from a number of limitations related to the reduced quantity, representativeness and resolution of the data, as well as poor rainfall control. The multi-technique (i.e., erosion pins, TLS, ground-based SfM photogrammetry) approach applied in this work at the Cardona salt diapir, with high spatial and temporal resolution, covering broad karren diversity, and combined with daily rainfall data (cumulative rainfall ≥730 mm), has allowed the assessment of the role of rainfall on solutional erosion. Slope-normal erosion normalized to 100 mm measured by the different methods consistently shows a mean value of around 10 mm, aligned with the rapid geomorphic evolution that characterizes these environments.

Differences in common measurement points across the different methods were below 4%, independently validating the data and techniques. The comparison of the implementation and performance of high-resolution TLS and photogrammetry using a conventional camera, suggests that the latter can be a more effective technique given its lower cost, simple data acquisition process, and more even distribution of data points, while the former could be more suitable for investigating large areas.

Point-specific erosion values normalized to 100 mm rainfall show significant variability controlled by the slope gradient and the intricate micro-topography that characterizes some karren features (e.g., solution flutes, solution runnels). Solutional erosion related to direct rainfall increases as the slope declines and the surface area that interacts with rainfall decreases. A linear regression between slope-normal erosion and slope shows that a 20° slope decline may involve an increase of around 2.7 mm in slope-normal erosion per 100 mm rainfall. The comparison of high-resolution point clouds shows the variability of slope-normal erosion within specific centimeter scale karren, which increases with micro-topography complexity. Simple solution bevels show a rather tight range of slope-normal erosion normalized to 100 mm at 7.5–14 mm, while the spectrum broadens to 0–22 mm and 0–30 mm in complex solution runnels and flutes, respectively. In solution bevels (i.e., rillenkarren), very rapid solutional erosion can occur along the slim and razor-sharp ridges because of the very high surface-to-volume ratio.

The observed general relationships between slope-normal erosion and both rainfall and slope can be used to model geomorphic evolution in rock salt exposures, including emergent salt domes where erosion is counterbalanced by diapiric rise. This approach has been illustrated with the case of the Bofia Gran depression at Cardona, estimating the annual salt volume removed by surface dissolution and restored by diapiric rise, using our erosion and uplift rate data, respectively. The greater contribution of salt rise is consistent with the geomorphology of the Bofia Gran, perched above the base-level and drained by a vadose canyon-like cave.

CRediT authorship contribution statement

Guillermo Pérez-Villar: Writing – review & editing, Writing – original draft, Methodology, Investigation, Conceptualization. **Francisco Gutiérrez:** Writing – review & editing, Writing – original draft, Supervision, Software, Resources, Methodology, Investigation, Funding acquisition, Conceptualization. **Alfonso Benito-Calvo:** Writing – review & editing, Software, Methodology, Investigation. **Carles Roqué:** Writing – review & editing, Investigation.

Declaration of competing interest

The authors declare that they have no known competing financial interests or personal relationships that could have appeared to influence the work reported in this paper.

Acknowledgements

This work has been developed by DIAPERNO Project (PID2021-123189NB-I00) funded by the Spanish Government (Ministerio de Ciencia e Innovación). GPV has a pre-doctoral contract (PRE2022-101600) co-financed by the Spanish Government (MCIN/AEI/10.13039/501100011033) and the European Social Fund (FSE+). GPV and FG belong to the IUCA research group of the Aragón Government. Authors are grateful to Mr. Ferrán Climent (Director of Catalunya Central Geoparc) for logistic support. We are grateful to two anonymous reviewers for their insightful comments and suggestions.

Appendix A. Supplementary data

Supplementary data to this article can be found online at https://doi.org/10.1016/j.geomorph.2026.110228.

Data availability

Data will be made available on request.

References

Alkattan, M., Oelkers, E.H., Dandurand, J.L., Schott, J., 1997. Experimental studies of halite dissolution kinetics, 1 the effect of saturation state and the presence of trace metals. Chem. Geol. 137 (3–4), 201–219.

Bögli, A., 1961. Karrentische, ein Beitrag zur Karstmorphologie. Zeit. Geomorph, NF 5, 185–193.

Bruthans, J., Asadi, N., Filippi, M., Vilhelm, Z., Zare, M., 2008. A study of erosion rates on salt diapir surfaces in the Zagros Mountains, SE Iran. Environ. Geol. 53, 1079–1089.

Bruthans, J., Filippi, M., Asadi, N., Zare, M., Slechta, S., Churackova, Z., 2009. Surficial deposits on salt diapirs (Zagros Mountains and Persian Gulf Platform, Iran): Characterization, evolution, erosion and the influence on landscape morphology. Geomorphology 107, 195–209.

Cardona, F., Viver, J., 2002. Sota la Sal de Cardona. Espeleo Club de Gracia, Barcelona.

De Waele, J., Gutiérrez, F., 2022. Karst Hydrogeology, Geomorphology and Caves. Wiley, Chichester.

De Waele, J., Picotti, V., Zini, L., Cucchi, F., Forti, P., 2009. Karst phenomena in the Cordillera de la Sal (Atacama, Chile). Geoacta 113–127.

De Waele, J., Picotti, V., Martina, M.L., Brook, G., Yang, L., Forti, P., 2020. Holocene evolution of halite caves in the Cordillera de la Sal (Central Atacama, Chile) in different climate conditions. Geomorphology 370, 107398.

Duffy, O., Hudec, M., Peel, F., Apps, G., Bump, A., Moscardelli, L., Dooley, T.P., Fernandez, N., Bhattacharya, S., Wislan, K., Shuster, M., 2023. The role of salt tectonics in the energy transition: an overview and future challenges. Tektonika 1 (1).

Font-Soldevila, J., 2006. Comportament de l'aigua subterrània a la vall Salada de Cardona. PhD Thesis, Universitat Politècnica de Catalunya. Departament d'Enginyeria Minera i Recursos Naturals, 152.

Frumkin, A., 1994. Hydrology and denudation rates of halite karst. J. Hydrol. 162 (1–2), 171–189.

Gaillardet, J., 2004. Denudation. In: Goudie, A. (Ed.), Encyclopedia of Geomorphology, 1. Routledge, New York, pp. 240–244.

Ginés, A., Lundberg, J., 2009. Rainpits: An outline of their characteristics and genesis. In: Ginés, À., Knez, M., Slabe, T., Dreybrodt, W. (Eds.), Karst Rock Features. Karren Sculpturing, 9. Založba ZRC, Ljubljana, pp. 169–184.

Glew, J.R., Ford, D.C., 1980. A simulation study of the development of rillenkarren. Earth Surface Processes 5 (1), 25–36.

Gulam, V., Gajski, D., Podolszki, L., 2018. Photogrammetric measurement methods of the gully rock wall retreat in Istrian badlands. Catena 160, 298–309.

Gunn, J., 2013. Denudation and erosion rates in karst. In: Shroder, J.F. (Ed.), Treatise on Geomorphology. In: Frumkin, A. (Ed.), Karst Geomorphology, 6. Elsevier, Amsterdam, pp. 72–81.

Gutiérrez, F., Ilyati, I., Zarei, M., 2025a. Surface karst geomorphology in the Jahani salt extrusion, Zagros Mountains, Iran. Geomorphology 485, 109859.

Gutiérrez, F., Haghighi, M.H., Ilyati, I., Motagh, M., del Val, M., 2025b. Diapiric and tectonic geomorphology of the river-damming Jahani salt extrusion associated with the strike-slip Kareh Bas Fault, including DInSAR displacement data (Zagros Mountains, Iran). Geomorphology 488, 109955.

Jackson, M.P.A., Hudec, M.R., 2017. Salt Tectonics: Principles and Practice. Cambridge University Press, Cambridge.

Jalali, L., Zarei, M., Gutiérrez, F., 2019. Salinization of reservoirs in regions with exposed evaporites. The unique case of Upper Gotvand Dam, Iran. Water Res. 157, 587–599.

James, M.R., Chandler, J.H., Eltner, A., Fraser, C., Miller, P.E., Mills, J.P., Noble, T., Robson, S., Lane, S.N., 2019. Guidelines on the use of structure-from-motion photogrammetry in geomorphic research. Earth Surf. Process. Landf. 44 (10), 2081–2084.

Lague, D., Brodu, N., Leroux, J., 2013. Accurate 3D comparison of complex topography with terrestrial laser scanner: Application to the Rangitikei canyon (NZ). ISPRS J. Photogramm. Remote Sens. 82, 10–26.

Lucha, P., Cardona, F., Gutiérrez, F., Guerrero, J., 2008. Natural and human-induced dissolution and subsidence processes in the salt outcrop of the Cardona Diapir (NE Spain). Environ. Geol. 53 (5), 1023–1035.

Lundberg, J., Ginés, À., 2009. Rillenkarren. In: Ginés, À., Knez, M., Slabe, T., Dreybrodt, W. (Eds.), Karst Rock Features. Karren Sculpturing, 9. Zalozba ZRC, Ljubljana, pp. 185–210.

Lupia-Palmieri, E., 2004. Erosion. In: Goudi, A. (Ed.), Encyclopedia of Geomorphology. Routledge, London, pp. 331–336.

Mirzaee, S., Pajouhesh, M., Imaizumi, F., Abdollahi, K., Gomez, C., 2024. Gully erosion development during an extreme flood event using UAV photogrammetry in an arid area, Iran. Catena 246, 108347.

Mottershead, D., Wright, J.S., Inkpen, R., Duane, W., 2007. Bedrock slope evolution in saltrock terrain. Z. Geomorphol. Suppl. 51 (1), 81–102.

Mottershead, D.N., Duane, W.J., Inkpen, R.J., Wright, J.S., 2008. An investigation of the geometric controls on the morphological evolution of small-scale salt terrains, Cardona, Spain. Environ. Geol. 53, 1091–1098.

Nadal-Romero, E., Revuelto, J., Errea, P., López-Moreno, J.I., 2015. The application of terrestrial laser scanner and SfM photogrammetry in measuring erosion and deposition processes in two opposite slopes in a humid badlands area (central Spanish Pyrenees). Soil 1 (2), 561–573.

Pérez-Villar, G., Gutiérrez, F., Zarroca, M., Roqué, C., Benito-Calvo, A., Menció, A., 2024. Late Quaternary morpho-stratigraphic record of diapir rise in the Cardona salt extrusion, NE Spain. Halokinetic sequences, raised terraces and uplift rates. Quat. Sci. Rev. 324, 108462.

Pérez-Villar, G., Gutiérrez, F., Bausilio, G., Di Martire, D., 2025a. Integrating DInSAR and detailed mapping for characterizing ground displacement in the Cardona salt extrusion related to diapiric uplift, disolutional lowering, landsliding and sinkholes. Eng. Geol. https://doi.org/10.1016/j.enggeo.2025.108068.

Pérez-Villar, G., Gutiérrez, F., Benito-Calvo, A., Roqué, C., 2025b. Morphometry and spatio-temporal evolution of salt karren. Earth Surf. Process. Landf. 50 (8), e70119.

Pueyo, J.J., 1975. Estudio petrológico y geoquímica de los Yacimientos potásicos de Cardona, Suria, Sallent y Balsareny (Barcelona, España). Unpublished PhD Thesis, Universidad de Barcelona.

Riba, O., Reguant, S., Villena, J., 1983. Ensayo de síntesis estatigráfica y evolutiva de la cuenca terciaria del Ebro. In: Ríos, J.M. (Ed.), Geología de España. Libro Jubilar IGME, 2, pp. 131–159.

Rosell, L., Pueyo, J.J., 1997. Second marine evaporitic phase in the South Pyrenean Foredee: the Priabonian Potash Basin (Late Eocene: Autochthonous–Allochthobous Zone). In: Busson, G., Schreiber, Ch. (Eds.), Sedimentary Deposition in Rift and Foreland Basins in France and Spain. Columbia University Press, New York, pp. 358–387.

Sans, M., 2003. From thrust tectonics to diapirism. The role of evaporites in the kinematic evolution of the eastern south Pyrenean front. Geol. Acta 1, 239–259.

Sans, M., Verges, J., 1995. Fold development related to contractional salt tectonics: Southeastern Pyrenean Thrust Front, Spain. In: Jackson, M.P.A., Roberts, D.G., Snelson, S. (Eds.), Salt Tectonics: A Global Perspective, 65. AAPG Memoir, pp. 369–378.

Talbot, C.J., Jackson, M.P.A., 1987. Internal kinematics of salt diapirs. AAPG Bull. 71 (9), 1068–1093.

Talbot, C.J., Medvedev, S., Alavi, M., Shahrivar, H., Heidari, E., 2000. Salt extrusion at Kuh-e-Jahani, Iran, from June 1994 to November 1997. In: Vendeville, B., Mart, Y., Vigneresse, J.L. (Eds.), Salt, Shale and Igneous Diapirs in and around Europe, 174. Geological Society, London, Special Publication, pp. 93–110.

Torra, O., Puig-Polo, C., Hürlimann, M., Latron, J., 2025. Analysis of erosive processes and erosion rate by in-situ measurements and multi-temporal TLS surveys in a mountainous badland area, Vallcebre (Spain). Catena 249, 108622.

Turowski, J.M., Cook, K.L., 2017. Field techniques for measuring bedrock erosion and denudation. Earth Surf. Process. Landf. 42 (1), 109–127.

Warren, J.K., 2016. Evaporites. A Geological Compendium. Springer, Cham, p. 1813.

Zarei, M., 2016. Factors governing the impact of emerged salt diapirs on water resources. Groundwater 54, 354–362.

Zarei, M., Raeisi, E., Talbot, C.J., 2012. Karst development on a mobile substrate: Konarsiah salt extrusion, Iran. Geol. Mag. 149 (3), 412–422.